

Visualization of blood-brain barrier disruption with dual-wavelength high-resolution photoacoustic microscopy

YONGCHAO WANG,^{1,3}  RUOXI ZHANG,^{1,3} QIAN CHEN,¹ HENG GUO,¹ XIAO LIANG,¹ TINGTING LI,¹ WEIZHI QI,^{1,2} AND LEI XI^{1,*} 

¹Department of Biomedical Engineering, Southern University of Science and Technology, Shenzhen, Guangdong, 518055, China

²Shenzhen Bay Laboratory, Shenzhen, 518132, China

³These authors contributed equally to this study

*xilei@sustech.edu.cn

Abstract: The blood-brain barrier (BBB) strictly regulates the substance exchange between the vascular network and the central nervous system, and plays a critical role in maintaining normal brain homeostasis. Impaired BBB is often accompanied with the emergence of cerebral diseases and probably further leads to severe neuroinflammation or even neurological degeneration. Hence, there is an urgent need to precisely monitor the impaired BBB to understand its pathogenesis and better guide the enactment of therapeutic strategies. However, there is a lack of high-resolution imaging techniques to visualize and evaluate the large-scale BBB disruption in pre-clinical and clinical aspects. In this study, we propose a dual-wavelength photoacoustic imaging (PAI) methodology that simultaneously reveals the abnormal microvasculature and impaired BBB within the cerebral cortex. In *in vivo* studies, BBB disruption in both mice and rats were induced by local hot-water stimulation and unilateral carotid arterial perfusion of hyperosmolar mannitol, respectively. Subsequently, the exogenous contrast agent (CA) was injected into the microcirculation *via* the tail vein, and photoacoustic (PA) images of the microvasculature and leaked CA within the cerebral cortex were obtained by dual-wavelength photoacoustic microscopy to evaluate the BBB disruption. Besides, analysis of distribution and concentration of leaked CA in lesion region was further conducted to quantitatively reveal the dynamic changes of BBB permeability. Furthermore, we exploited this approach to investigate the reversibility of BBB disruption within the two distinct models. Based on the experimental results, this new proposed approach presents excellent performance in visualizing microvasculature and leaked CA, and enabling it possesses great potential in evaluating the abnormal microvasculature and impaired BBB result from cerebrovascular diseases.

© 2022 Optica Publishing Group under the terms of the [Optica Open Access Publishing Agreement](#)

1. Introduction

Blood-brain barrier (BBB), existing at all-levels cerebral vasculatures, is formed by cerebral vascular endothelial cells, and strictly separates the central nervous system from blood circulation [1–3]. An intact BBB is essential for maintaining stable micro-environment and normal brain function [4]. Numerous investigations have demonstrated that increased BBB permeability is not only a significant hallmark of the morbidity of various cerebral diseases, including stroke, brain tumor, epilepsy, cerebral malaria and Alzheimer's diseases, but also has been directly linked to the pathogenesis of neuronal inflammation and degeneration [5–10]. Hence, it is of great importance to realize *in vivo* visualization of BBB disruption, which enables us establish a comprehensive understanding of the pathogenesis of cerebral diseases. To date, a wide range of advanced imaging methodologies have been established to evaluate the BBB disruption, basing

on detecting the leakage of endogenous components (Albumin, immunoglobulin and fibrinogen et al.) or exogenous CA (Evans blue, fluorochromes and radiotracers et al.) [11].

Among these methodologies, immunochemistry and immunofluorescence are the gold standard for detecting the BBB disruption, however, require the preparation of *ex vivo* sample of brain, which limits its application in revealing the dynamic process of BBB disruption [12,13]. Magnetic resonance imaging (MRI), single photon emission computed tomography (SPECT) and positron emission computed tomography (PET) scanners are the widely applied techniques in both clinical and pre-clinical stage, profiting from their predominant capacity of noninvasive whole-brain detection [14–16]. Nevertheless, they more or less suffer from ionizing radiation, low spatial resolution, poor signal-to-noise ratio (SNR), and expensive cost. A great number of optical imaging modalities have been developed to visualize the impaired BBB and microvasculature in pre-clinical studies, including Near-Infrared fluorescence imaging (NIR-FI), confocal microscopy, laser speckle contrast imaging (LSCI), spectral imaging and optical coherence tomography angiography (OCTA) [17–21]. Although NIR-FI owns significant dominance in imaging speed, field of view (FOV) and operation, its spatial resolution and SNR are still insufficient for precisely identifying the lesion region, especially within the strong optical scattered tissues. The *in vivo* confocal microscopy possesses unbeatable spatial resolution with limited FOV and temporal resolution, prevents it from visualizing the dynamic changes of BBB permeability. Other optical imaging modalities, such as LSCI and spectral imaging are lack of the depth resolved capability.

Based on PA effect, PAI reconstructs the image by detecting the ultrasound signal generated by the optical absorption of the target, simultaneously possessing the abundant contrast and spectral features of optical imaging and deep imaging depth of ultrasound imaging [22,23]. Due to its unique superiority in visualizing blood vessels, PAI has been widely exploited to investigate the vascular aberrations result from cerebral diseases [24–28]. Besides, the novel mechanism of optical absorption also enables PAI have a promising prospect in *in vivo* monitoring the BBB disruption, especially when combined with the specific CA [29]. As demonstrated in previous reports, photoacoustic computed tomography (PACT) and acoustic resolution photoacoustic microscopy (AR-PAM) have been reported for monitoring the impaired BBB induced by cerebral diseases with considerable penetration depth [30–32]. However, the limited spatial resolution prevents it capability of precisely evaluating the BBB disruption and disclosing the abnormal microvasculature.

To better address these issues mentioned above, as shown in Fig. 1, we proposed a high-resolution dual-wavelength photoacoustic microscopic modality that allows us simultaneously capture the microvascular network and distribution of leaked CA within whole cerebral cortex in rodents, providing more comprehensive information about BBB disruption and cerebral diseases. When compared with conventional NIR-FI, it displays a more superior capability in spatial resolution and SNR for *in vivo* visualizing the BBB disruption. Based on the proposed methodology, we firstly investigated the local BBB disruption in mice and large-scale BBB disruption in adult rats, respectively. Furthermore, quantitative analysis of distribution and concentration of the leaked CA was conducted at different time points, revealing that the local BBB disruption in mice is gradually deteriorating within 4 hrs post model. In addition, we further investigated the reversibility of mentioned BBB disruption, which demonstrates that local disruption in mice is irreversible while the large-scale disruption in rats is reversible. In summary, the observed results indicate that the proposed PA method has promising prospect in the investigation of BBB disruption.

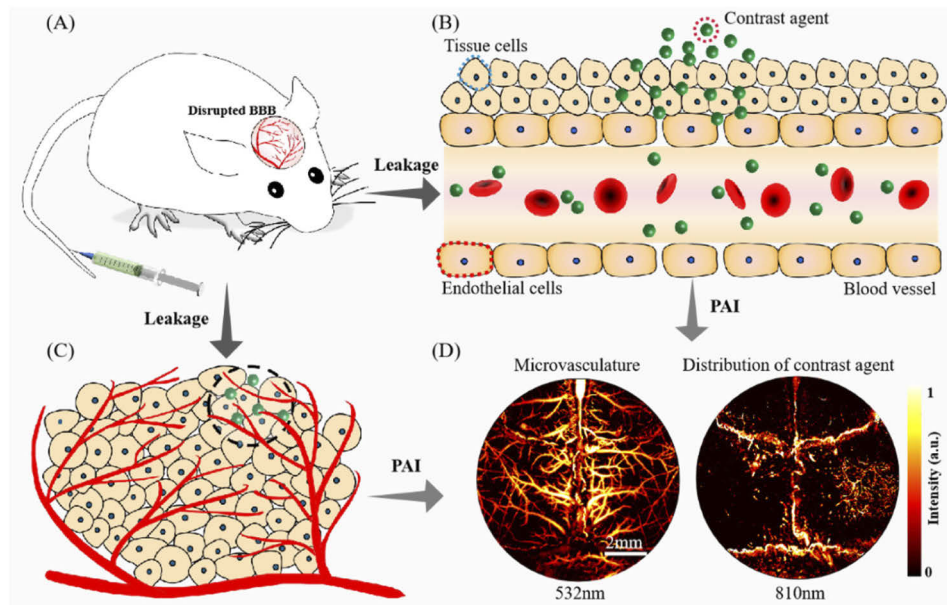


Fig. 1. High resolution visualization of BBB disruption based on dual-wavelength photoacoustic microscopy (OR-PAM). (A) An experimental animal with disrupted BBB is administrated with exogenous CA *via* tail vein. (B) The CA penetrates the disrupted BBB into the brain parenchyma within the lesion region. (C) Schematic diagram of the leaked CA around aberrant blood vessels. (D) The PA images of microvasculature (left) and distribution of leaked CA (right) obtained from a mouse with disrupted BBB.

2. Materials and methods

All the experimental protocols were approved and supervised by the Animal Ethics Committee at the Southern University of Science and Technology (SUSTech). Before surgery, all animals were kept in an environmentally controlled breeding room with adequate food and water, and a 12-hour light-dark interval.

2.1. Animal preparation

Hot water stimulation. This model is further improved from previous reports [33,34]. Briefly, female BALB/c mice (8–10 weeks old, 20–30 g) were deeply anesthetized by intraperitoneal injection of chloral hydrate (50 mg/ml, 5 ml/kg) and then placed into a homemade stereotactic frame. Body temperature was continuously monitored and maintained at 37.5 °C with a self-feedback heating pad. An incision over the midline of scalp was cautiously made, followed with the exposure of the skull by removing superficial fascia with sterile cotton swabs. Subsequently, dental cement was applied to cover the whole skull, only leaving an exposed region with a diameter of 2 mm in the right hemisphere. Finally, the exposed region was treated with hot water droplets for ten minutes, at a rate of 0.03 mL/s and a temperature of 50°C. These treated mice were further divided into two groups: 1) Model group: mice were injected with CA solution *via* tail vein immediately post hot water stimulation and were imaged with OR-PAM and NIR-II fluorescence systems before and 1 hr, 2 hrs, and 4 hrs post the injection. 2) Model_24 h group: mice were injected with CA solution *via* tail vein 24 hrs post the hot water stimulation and were imaged 4 hrs after the injection.

Intracarotid perfusion of mannitol. Female SD rats (8–10 weeks old, 220–250 g) were deeply anesthetized by intraperitoneal injection of chloral hydrate (50 mg/ml, 5 ml/kg) and placed into a

commercial stereotactic frame. All rats were further divided into three groups: model group, sham-operated group, and control group. 1) Model group: rats were administrated CA solution *via* tail vein immediately after intracarotid perfusion of mannitol; 2) Sham-operated group: rats were administrated CA solution *via* tail vein immediately after separation of carotid artery; 3) Control group: rats were ipsilaterally perfused with mannitol but injected with equivalent physiological saline. Specifically, the unilateral BBB disruption was induced by perfusion of mannitol through the left carotid artery, as described in previous reports [35–37]. Briefly, a 2–3 cm vertical incision was made from the suprasternal notch to below the chin. After separation of the subcutaneous muscle and membranes, the common carotid artery (CCA), the bifurcation of internal carotid arteries (ICA) and the external carotid artery (ECA) were exposed. A polyethylene catheter (PE 10) was inserted into the ECA toward the bifurcation, following the clipping of CCA and ECA. Then, the hyperosmolar mannitol solution (25%, 2 ml) was injected into left hemisphere through released ECA with a rate of 0.033 ml/s. After perfusion, the proximal stump of the ECA was tightly ligated and the proximal stump of the CCA was released. These treated rats were further divided into model group and model_24 h group to verify the reversibility of the model. 1) Model group: rats were injected with CA solution *via* tail vein immediately post the perfusion. 2) Model_24 h group: rats were injected with CA solution *via* tail vein 24 hrs post the perfusion. Before imaging, a craniotomy was performed for all rats, then the exposed cortex was imaged with OR-PAM and NIR II fluorescence systems.

2.2. Imaging system

All data in this study are derived from a commercial OR-PAM system (VIS-50-NIR, PAOMTek Inc., Chengdu) and a commercial NIR-II system (Series III 900/1700-D NIR-II, Yingrui, Suzhou). The schematic of the OR-PAM system is shown in [Supplement 1](#). As depicted by the absorption spectra, the hemoglobin and CA have strong absorption at 532 nm and 810 nm, respectively ([Supplement 1](#)). Hence, lasers with these two wavelengths are used as excitation sources to capture the blood vessels and distribution of CA within cerebral cortex. The OR-PAM system has an imaging speed of 20 s with a circular imaging domain of up to 10 mm in diameter. And the systemic lateral, axial resolutions and imaging depth are about 10 μm , 110 μm , and 800 μm , respectively. For *in vivo* fluorescence imaging, the NIR-II system provides a lateral resolution of 30 μm and a 500 ms exposure time is chosen to evaluate the distribution of CA.

2.3. Ex vivo assessment

Evans Blue injection. Post BBB disruption, the azo dye solutions (Evans Blue, 2%, 0.1 ml for mice and 1.2 ml for rats, respectively) were slowly injected *via* tail vein. The *ex vivo* brains were taken from rats and mice 4 hrs post the injection of azo dye and used to further validate BBB disruption based on the leakage of Evans Blue.

Pathological examination of brain section. Post BBB disruption, mice and rats were deeply anesthetized with isoflurane and then decapitated. The brains were quickly removed from the skull and immediately placed into ice-cold 4% paraformaldehyde universal tissue fixative (Biosharp, Anhui). The *ex vivo* samples were further fixed with 4% paraformaldehyde. Subsequently, the samples were trimmed, dehydrated, embedded, sectioned, stained, and mounted in strict accordance with the Standard Operation Procedure (SOP) of the pathological experiment. The slice images were collected by a panoramic slice scanner (CaseViewer2.4, 3DHISTECH, Hungary), and the results were generated by a scanning and browsing software (PANNORAMIC DESK/MIDI/250/1000, 3DHISTECH, Hungary).

2.4. Contrast agent preparation

The contrast agent was composed of a previously used semiconducting polymer (SP2) and a commercial NIR-II fluorescent dye (TTQ-F), functionalized with a lipid-polyethylene glycol (PEG)

molecule, 1,2-Distearoyl-*sn*-glycero-3-phosphoethanolamine-*N*-[methoxy(polyethyleneglycol)-2000] (DSPE-PEG₂₀₀₀) [29]. The SP2 polymer was synthesized according to the procedure described in previous reports [38,39]. The TTQ-F was purchased from Biodrvier Technology inc. (Shanghai, China). The DSPE-PEG₂₀₀₀ was purchased from Nanocs (USA). The chemical structure and absorption spectrum of SP2 and TTQ-F were shown in [Supplement 1](#).

The process started with the preparation of a THF solution (1 mL) containing SP2 (0.5 mg), TTQ-F (0.5 mg) and DSPE-PEG₂₀₀₀ (2 mg). The THF solution was then added to 9 mL of double distilled (DD) water and sonicated continuously for 2 minutes with a probe sonicator at 75 W output. THF was removed through dialysis against DD water for 2 days, and the solution was filtered through a 0.2 µm syringe filter to yield nanoparticles suspended in water.

After the above steps, SP2 and TTQ-F would be encapsulated by DSPE-PEG₂₀₀₀ into water-soluble core-shell nanoparticles. Since SP2 and TTQ-F have strong absorbance at 810 nm, we ultimately obtained a photoacoustic/red-emitting dual-modal CA.

2.5. Data analysis

All photoacoustic images were reconstructed using a custom-built script in MATLAB 2016b (The MathWorks, USA). All statistics graphs were generated by GraphPad Prism 6 (GraphPad Software Inc., USA). When calculating the distribution of leaked CA, the region with uniformly distributed CA was manually selected, and distribution was derived by calculating the number (N1) of pixels within the selected region. When calculating the concentration of leaked CA, an appropriate threshold was chosen to filter out of background noise. Then, number (N2) of CA was calculated by counting the pixels with larger amplitude than threshold within the selected region. Finally, the concentration (C) of leaked CA can be calculated as:

$$C = \frac{N2}{N1}$$

3. Results

3.1. In vivo evaluation of local BBB disruption in mouse with intact skull

We firstly evaluate the feasibility of PA methodology by *in vivo* monitoring the local BBB disruption in the mouse with unilateral hot water stimulation. Figure 2(A) presents the merged PA images of the cortical microvasculature and CA distribution obtained before and 1 hr, 2 hrs, 4 hrs post the CA injection, in which the gray color represents the microvasculature, and hot color indicates the CA distribution. As shown in Fig. 2(A)(i), we can only obtain the information of microvasculature without CA injection, although local BBB disruption has been successfully induced within the right hemisphere. But post the injection, we can clearly observe that the leaked CA, in terms of range and amount, is gradually accumulating within the local region in the right hemisphere, which indicates that the BBB disruption is dynamically changing post hot water stimulation, as shown in Figs. 2(A)(ii-iv). To further verify the accuracy and superiority of the PAI method, conventional NIR II fluorescence imaging was also performed for the same mice at the corresponding time points. As shown in Figs. 2(B)(i-iv), the variation tendency of the leaked CA revealed by fluorescence imaging is well consistent with that of PA imaging, proving the validity of our proposed method. Figure 2(C) presents a typical photograph of an *ex vivo* brain taken from a mouse with unilateral hot water stimulation 4 hrs post the injection of Evans blue. The leakage of Evans blue within lesion region also provides a solid support for the accuracy of PA method. Figures 2(D)–2(F) are the close-up views of the lesion region indicated by white dotted circles in Fig. 2(C), Fig. 2(B)(iv), and Fig. 2(A)(iv), respectively. It is obvious that the PA image can provide more detailed information of BBB disruption and microvasculature, when compared with that of fluorescence image and *in vitro* evaluation.

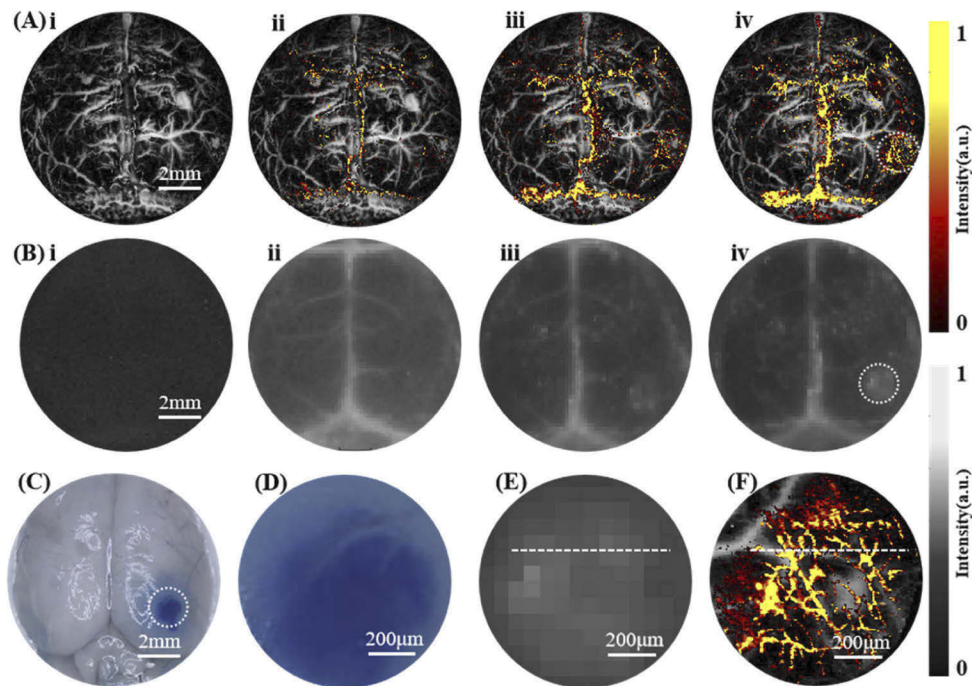


Fig. 2. *In vivo* PA evaluation of local BBB disruption in the mouse with intact skull. (A) The merged PA images of microvasculature and CA distribution in a mouse with hot-water stimulation. (i-iv) Images were obtained before and 1 hr, 2 hrs, 4 hrs post CA injection. (B) NIR II fluorescence images of CA distribution within the same mouse obtained at corresponding time points. (C) Photograph of an *ex vivo* brain taken from a mouse with hot-water stimulation 4 hrs post injection of Evans blue. (D) Magnified photograph of the region marked with a dotted circle in C. (E) Magnified image of the lesion region marked with a dotted circle in B (iv). (F) Magnified image of the lesion region marked with a dotted circle in A (iv).

To better illustrate the performance difference between PA and fluorescence imaging, two profiles were derived from Figs. 2(E)–2(F) at corresponding locations marked by white dotted lines, as shown in Fig. 3(A). The black and gray curves present profiles extracted from fluorescence and PA images, respectively, which indicates that PA methodology possesses a better spatial resolution. Besides, we also conducted quantitative analysis of the signal-to-background ratio (SBR) of the two images, as shown in Fig. 3(B). It can be clearly observed that the SBR of PA methodology is superior to that of fluorescence image.

In addition, we further investigated the time dependence of BBB disruption by quantitatively analyzing the dynamic changes of CA distribution and concentration, representing the range and severity of BBB disruption, respectively. Figure 3(C) presents the statistical data of distribution range of the leaked CA, in which the black and gray histograms are derived from fluorescence and PA images, respectively. The results demonstrate that CA distribution is gradually increasing but with a reduced speed within 4 hrs, and the corresponding increments are 78%, 22% in the first and second two hours, respectively, which indicates the region of BBB disruption will gradually stabilize. Figure 3(D) presents the quantitative analysis of the concentration of the leaked CA in both control and treat hemispheres. Accordance with CA distribution, the concentration in the treated hemisphere increases immediately after CA injection with a higher accumulated rate. For instance, the concentration of CA increased by 42% in the first two hours, while the increment

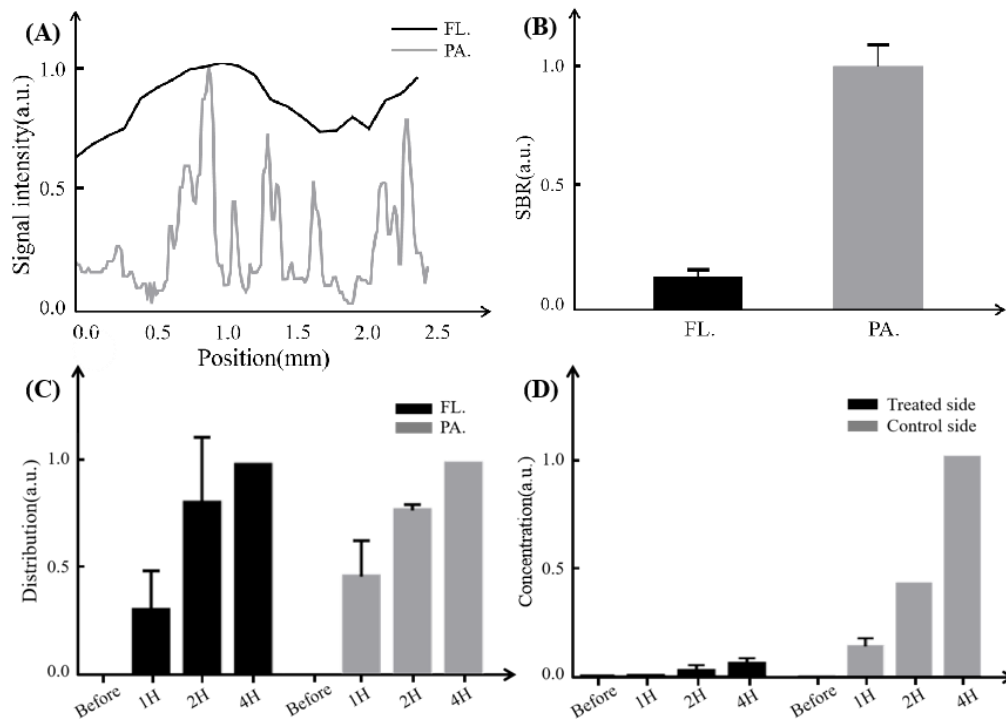


Fig. 3. Quantitative analysis of both PA and fluorescence images. (A) Profiles derived from the locations indicated by white dotted lines in Figs2. E-F, respectively. (B) Normalized SBR. (C) Quantitative analysis of the CA distribution in the treated side of NIR II fluorescence images and PA images, respectively. (D) Quantitative analysis of the CA concentration in the treated and control sides of PA images. Data represent as mean with s.d. ($n=3$ for all groups). FL., fluorescence; PA., photoacoustic.

in the second two hours remained at 58%, revealing that the severity of BBB disruption was gradually deteriorating within 4 hrs. On the contrary, the concentration of control hemisphere with intact BBB scarcely changes.

3.2. Evaluation of large-scale BBB disruption in rat

To validate the extensive applicability of the PA methodology, we investigated the large-scale BBB disruption in adult rats treated with unilateral carotid arterial perfusion of hyperosmolar mannitol. Figures 4(A)(i-iii) denote the merged PA images of the microvasculature and leaked CA in the cerebral cortex captured at 24 hrs post the injection. As shown in Fig. 4(A)(i), distribution of the leaked CA in the treated hemisphere of the model group is significantly higher than that of the contralateral hemisphere, especially in the marginal regions of cerebral cortex. When integrated with distribution of microvasculature, we can notice that the leakage of CA is more concentrated in terminal vessels away from sagittal sinus. We can infer that the BBB integrity of micro-vessels may be more prone to collapse than that of mesoscopic vessels under acute hyperosmotic environment. Interestingly, there also exists slight leakage in the control hemisphere, revealing that a weak BBB disruption has also been triggered simultaneously. A possible explanation is that the perfused mannitol fully mixed with blood after cardiac circulation, which increased the global osmotic pressure of microvascular system, eventually resulted in moderate disruption of BBB integrity in the right hemisphere [40,41]. Figures 4(A)(ii) demonstrates that there

exists no significant distribution of CA in the bilateral hemispheres of the sham-operated group, which is well consistent with the intact BBB of rats in the sham-operated group. As predicted, although BBB integrity of left hemisphere has been destroyed in the control group, we cannot extract any information related to BBB disruption due to the lack of CA injection, as depicted in Fig. 4(A)(iii).

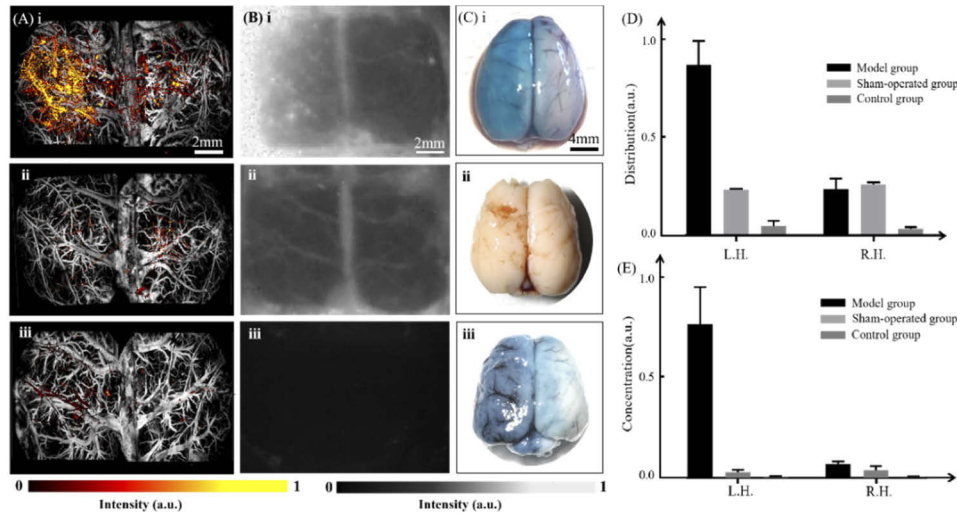


Fig. 4. *In vivo* PA evaluation of large-scale BBB disruption in the rat induced by carotid arterial perfusion of mannitol. (A) The PA images of microvasculature and CA distribution obtained 24 hrs post the injection in rats with exposed cortex. (i-iii) Images were obtained from model group, sham-operated group and control group, respectively. (B) NIR II fluorescence images obtained in corresponding rats. (C) Photographs of *ex vivo* brains taken from corresponding rats 24 hrs post the injection of Evan blue. (D) Quantitative analysis of the CA distribution in the left and right hemispheres from PA images. (E) Quantitative analysis of the CA concentration in the left and right hemispheres from PA images. Data represent as mean with s.d. ($n = 3$ for all groups). L.H., left hemisphere; R.H., right hemisphere.

Fluorescence images were also obtained in corresponding rats to further verify the findings mentioned above, as shown in Figs. 4(B)(i-iii). Well consistent with PAI, CA appears to accumulate significantly in the perfused hemisphere of model group, while it is almost undetectable in contralateral hemisphere. On the contrary, distribution of CA in both hemispheres of sham-operated group shows no obvious difference, and mainly accumulates in several mesoscopic vascular branches. As shown in Fig. 4(B)(iii), the fluorescence image obtained from the control group is almost vacant, providing no information accessing to BBB disruption. Figures 4(C)(i-iii) present the typical photographs of *ex vivo* brains taken from rats of three groups 24 hrs post the injection of Evans blue, which are presented for the purpose of validating whether the BBB is intact or disrupted.

We further carried out quantitative analysis of the distribution and concentration of the leaked CA to better illustrate the significant difference of BBB disruption among three groups. Figure 4(D) presents the normalized distribution range of CA in each hemisphere. We can observe that the distribution range of the treated hemisphere in the model group is about 3.7 times higher than that of the contralateral hemisphere. Apart from the model group, both hemispheres of sham-operated group possess the similar distribution range which is a quarter of the treated hemisphere. Besides, distribution range of control group only remains at 3% compared with that of the model group, which may result from the absorption of 810 nm laser by blood vessels.

Figure 4(E) shows the normalized concentration of CA over the corresponding hemispheres. As expected, the treated hemisphere in the model group owned the highest concentration of CA, indicating the most severe BBB disruption has been induced over that region. A lower concentration in the control hemisphere is also well consistent with the weaker BBB disruption as discussed above. The calculated concentration of another two groups is also negligible compared with that of the treated hemisphere in the model group. Hence, both the images and quantitative analysis demonstrate that the proposed PA methodology can be well applied to evaluating large-scale BBB disruption.

3.3. Reversibility of BBB disruption

As shown in Fig. 5, we further assessed the reversibility of two distinct BBB disruption by comparing the severity of CA leakage within 24 hrs and 48 hrs post the establishment of the model. As depicted in Figs. 5(A)(i-ii), the merged PA images indicate that local BBB disruption in mice has been successfully induced within the treated side in both groups. Figures 5(B)(i-ii) show the close-up views of the treated region marked by white dotted circles in Figs. 5(A)(i-ii), respectively. Figure 5(C) presents the corresponding fluorescence images in same rats, which agrees well with the results in Fig. 5(A). The comparison of CA leakage of both hemispheres in model_24 h group is presented in Fig. 5(D), which reveals that both distribution and concentration of leaked CA in the treated side are far beyond that of the control side (around $\pm 64\%$, $\pm 72\%$, respectively). When compared with model group, it exhibits a similar distribution (around $\pm 1.4\%$) and concentration (around $\pm 6.7\%$) of the leaked CA in the treated side, which indicates that the rate of CA release maintains at a constant level within 48 h, reflecting the BBB disruption induced by hot water stimulation is probably irreversible. On the contrary, the phenomenon observed in rats with unilateral carotid arterial perfusion of hyperosmolar mannitol is diametrically distinct. As shown in Figs. 5(F)(i-ii), although leaked CA in the treated side of model_24 h group appears to be higher than that of the control side, it remains at a relatively low level when compared with that of the model group, which is well verified by the fluorescence images presented in Figs. 5(G)(i-ii). Additionally, as shown in Fig. 5(H), both two quantitative parameters in the treated hemisphere are obviously higher than that of the control hemisphere (around $\pm 62\%$ and $\pm 50.8\%$, respectively), which indicates a BBB disruption has been induced in the treated side. It is worth noting that although the treated hemisphere of model_24 h group possesses a similar distribution region (around $\pm 5\%$), the CA concentration is far from comparable (around $\pm 59.2\%$), when compared with that of the model group. This phenomenon demonstrates that the BBB disruption induced by unilateral carotid arterial perfusion of hyperosmolar mannitol is gradually recovering within 48 h, which agrees well with the previous reports [42,43].

3.4. Pathological analysis of the lesion region

Supplement 1 presents the pathological images of coronal planes that across the lesion regions in both mouse and rat. As shown in Supplement 1, significant tissue defect can be observed in the treated hemisphere, and brain tissue around the defect appears slight structural looseness, accompanied with vast small cavities (red arrow) and enlarged neuronal gap (yellow arrow). The pathological result indicates that permanent damage is induced by hot water stimulation within the lesion region, which maybe a potential explanation for the irreversibility of BBB disruption in mouse. On the contrary, there exists no obvious difference between the two hemispheres in the rat as shown in Supplement 1. And the close-up views indicates that tissue within the lesion region presents normal pathological morphology, in terms of compact structure and proper neuronal gap [43]. We can conclude that hyperosmotic mannitol induces acute BBB disruption but without significant tissue damage, which makes it possible for the recovery of BBB integrity.

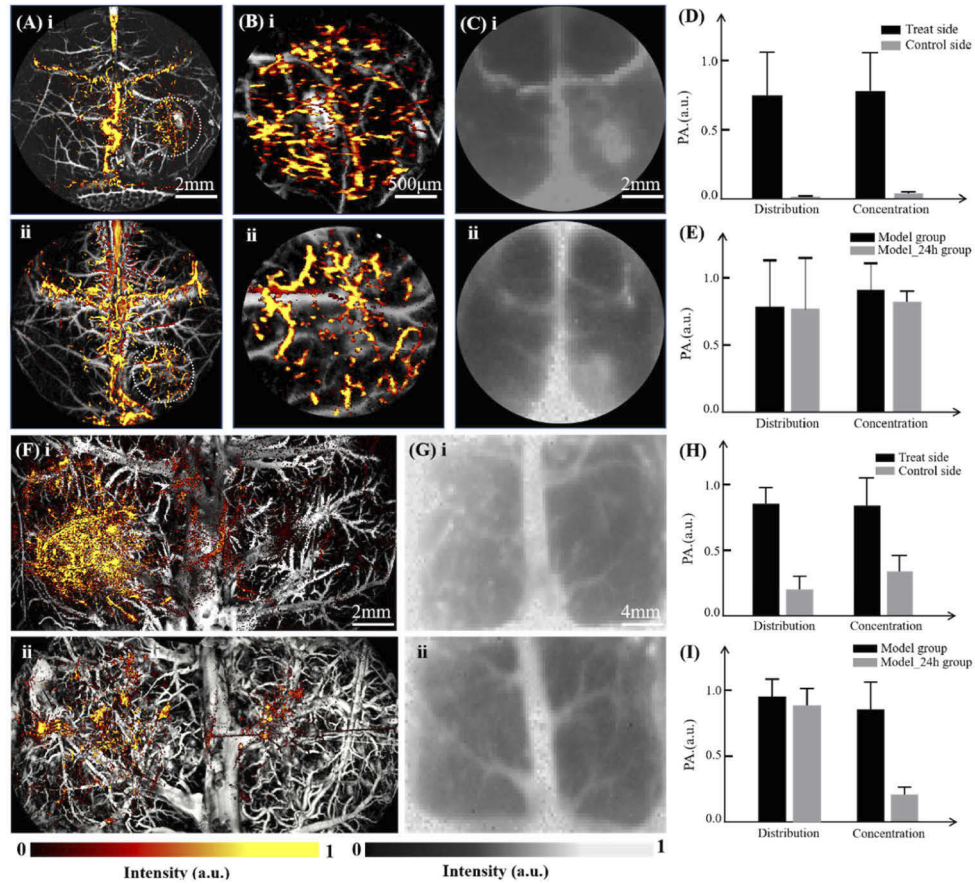


Fig. 5. Reversibility of BBB disruption. (A) Merged PA images of the microvasculature and CA distribution in mice. (B) Magnified images of the region indicated by dotted circles in A(i-ii). (C) NIR II fluorescence images, (i) model group. (ii) model_24 h group. (D) Quantitative analysis of the CA distribution and concentration of control and treated sides in the model_24 h group. (E) Quantitative analysis of the CA distribution and concentration of the treated side in model and model_24 h groups. (F) Merged PA images of microvasculature and CA distribution in rats. (G) Corresponding NIR II fluorescence images, (i) model group. (ii) model_24 h group. (H) Quantitative analysis of the CA distribution and concentration of control and treated sides in the model_24 h group. (I) Quantitative analysis of the CA distribution and concentration of the treated side in model and model_24 h groups. Data represent as mean with s.d. (n= 3 for all groups).

4. Discussion

A wide range of cerebral diseases are tightly associated with impaired BBB and abnormal microvasculature. The dynamic nature of cerebral diseases leads to the variation of these two affected structures at different time points. Therefore, precisely measuring these two structures can provide comprehensive information related to pathology of cerebral diseases, allowing us to distinguish the “tissue-at-risk” from normal tissue. Over the past decades, various imaging techniques have been exploited to evaluate BBB disruption by measuring the leakage of BBB nonpermeable tracers in both clinical and preclinical stages. Regrettably, these imaging methodologies usually suffer from either low resolution, limited FOV or lack of depth resolved information [6,20,44–46]. Besides, few of them can provide detailed messages access to distorted microvasculature, which is another crucial characteristic related to cerebral diseases [20,45]. Here, we proposed a dual-wavelength photoacoustic imaging methodology for *in vivo* visualizing the changes of microvasculature and BBB permeability within the lesion region. To verify the superior capability of our proposed methodology, we firstly performed experiments in mice with local BBB disruption. As discussed in section 3.1, the PA method allows to measure the microvasculature and BBB disruption with more superior capabilities in spatial resolution and SBR when compared with conventional fluorescence imaging. By combining with quantitative approach, this method is further applied to reveal distinct features of BBB disruption.

Increased BBB permeability does not exist only as a side effect, it can also be applied as an effective tool in the treatment of cerebral diseases [47,48]. As previously reported, BBB integrity could be artificial disrupted by diverse techniques, such as highly focused ultrasound, photochemical internalization (PCI) and photodynamic therapy (PDT), for enhancing drug uptake in targeted region to realize brain disease therapy [49–51]. However, the artificial BBB opening only maintains a short time-window, and its severity changes significantly as time goes on [52]. Hence, it is vital to monitor the time course of BBB opening for determining the optimal time for drug release. To illuminate the continuous imaging capability of our PA technology, we further examined the time-dependence of BBB disruption in mice by quantitatively measuring the distribution and concentration of the leaked CA at four different time points. We observed that the increasement of CA distribution in the first two hours is about 3.8 times larger than that of the second two hours. While, increasement of CA concentration in second two hours is 1.38 times large than that of the first two hours, indicating that although the extent of BBB disruption tends to be stable, its severity is gradually deteriorating within 4 hours. We also noticed that the leakage of CA in the second day post the establishment of the model is comparable with that of the first day. A possible explanation could be that BBB disruption induced by hot water stimulation is irreversible, which may result from the permanent tissue damage in the lesion region. Secondly, we further conducted experiments to test the applicability of the PA methodology in evaluating large-scale BBB disruption induced by hyperosmolar mannitol. As presented in section 3.2, we observe that the leaked CA is more concentrated in cerebral regions away from the sagittal sinus. We can infer that BBB integrity of different vessels is distinct, and micro-vessels is more easily to collapse than mesoscopic vessels within the acute hyperosmotic environment. Besides, we observe that the distribution of the leaked CA in the second day is similar to that of the first day (around $\pm 5\%$), but the concentration is significantly decreased (around $\pm 59.2\%$). A potential explanation is that the effect of hyperosmotic environment on BBB permeability is modest and reversible, allowing the BBB to gradually return to normal condition within 2 days.

Although this study demonstrates the superior capability of the proposed dual-wavelength OR-PAM in evaluating BBB disruption, there are further improvements to optimize the methodology. Firstly, it is possible to enhance its capability in acquiring information along depth direction by using a longer wavelength laser. The imaging depth is less than 1 mm in this study, only making it accessible to superficial cortex. However, the BBB disruption resulting from cerebral diseases does not only exist in cortex, but also in several deep brain regions, such as hippocampus,

amygdala and cerebellum [12,53–55]. By combining longer wavelength laser (e.g., NIR II) with corresponding CA, a higher imaging depth beyond cortex could be achieved. In addition, it is possible to exploit dual-modality photoacoustic imaging system that integrates PACT with existing OR-PAM, simultaneously realizing high resolution cortical evaluation and high-depth coronal plane evaluation. A desired imaging depth at centimeter scale allows us realize whole-brain evaluation of BBB disruption in fundamental brain studies.

Secondly, functional parameters related to blood flow need further exploration to investigate the constitutive relationships among microvasculature, BBB disruption and cerebral diseases. Normal blood flow within the brain is well controlled by metabolic demands to execute normal physiological activities. Generally, cerebral diseases are also tightly associated with abnormal blood flow, in terms of decreased hemoglobin oxygen saturation, impaired blood supply and distorted microvasculature. Further analyzing approaches need to be established to extract the flow velocity of targeted vessels. In addition, multispectral PA methodology can be exploited by introducing other wavelengths (e.g., 540–560 nm) to calculate the oxygen saturation inside the lesion region, allowing us to analyze the regional metabolic abnormality induced by cerebral diseases. With the assistance of extra messages mentioned above, we can better investigate the correlation between abnormal microvasculature and BBB disruption, making it more suitable to understand the pathogenesis of cerebral diseases.

5. Conclusion

In this work, we proposed a dual wavelength PA microscopic methodology for *in vivo* visualizing the BBB disruption and distorted microvasculature induced by cerebral diseases. By comparing with conventional NIR-II fluorescence imaging, we verified its superior capability in SBR and spatial resolution. Additionally, we further applied this technique to evaluate the local and large-scale BBB disruption within distinct model, successfully revealing their time dependence and reversibility, respectively. These results demonstrate that the proposed PA method is a promising tool for *in vivo* investigation of the changes in BBB permeability and microvasculature associated cerebral diseases.

Funding. National Natural Science Foundation of China (62022037, 62105140, 61775028, 81571722, 61528401); Department of Science and Technology of Guangdong Province (2019ZT08Y191, SZBL2020090501013); Guangdong Provincial Department of Education (2021ZDZX1064); Shenzhen Science and Technology Program (JCYJ20200109141222892, KQTD20190929172743294); Startup grant from Southern University of Science and Technology.

Disclosures. The authors declare no conflicts of interest.

Data availability. Data underlying the results presented in this paper are not publicly available at this time but may be obtained from the authors upon reasonable request.

Supplemental document. See [Supplement 1](#) for supporting content.

References

1. R. Daneman, "The blood-brain barrier in health and disease," *Ann. Neurol.* **72**(5), 648–672 (2012).
2. N. J. Abbott, L. Ronnback, and E. Hansson, "Astrocyte-endothelial interactions at the blood-brain barrier," *Nat. Rev. Neurosci.* **7**(1), 41–53 (2006).
3. R. Daneman and A. Prat, "The blood-brain barrier," *Cold Spring Harb. Perspect. Biol.* **7**(1), a020412 (2015).
4. N. J. Abbott, A. A. Patabendige, D. E. Dolman, S. R. Yusof, and D. J. Begley, "Structure and function of the blood-brain barrier," *Neurobiol. Dis.* **37**(1), 13–25 (2010).
5. Y. Gursoy-Ozdemir, M. Yemisci, and T. Dalkara, "Microvascular protection is essential for successful neuroprotection in stroke," *J. Neurochem.* **123**(2), 2–11 (2012).
6. S. Tiwary, J. E. Morales, S. C. Kwiatkowski, F. F. Lang, G. Rao, and J. H. McCarty, "Metastatic brain tumors disrupt the blood-brain barrier and alter lipid metabolism by inhibiting expression of the endothelial cell fatty acid transporter Mfsd2a," *Sci. Rep.* **8**(1), 8267 (2018).
7. D. Janigro, "Are you in or out? Leukocyte, ion, and neurotransmitter permeability across the epileptic blood-brain barrier," *Epilepsia* **53**(1), 26–34 (2012).
8. A. P. Sagare, R. D. Bell, and B. V. Zlokovic, "Neurovascular dysfunction and faulty amyloid beta-peptide clearance in Alzheimer disease," *Cold Spring Harb. Perspect. Med.* **2**(10), a011452 (2012).

9. M. Lu and G. Hu, "Targeting metabolic inflammation in Parkinson's disease: implications for prospective therapeutic strategies," *Clin. Exp. Pharmacol. Physiol.* **39**(6), 577–585 (2012).
10. A. Chodobski, B. J. Zink, and J. Szmydynger-Chodobska, "Blood-brain barrier pathophysiology in traumatic brain injury," *Transl. Stroke Res.* **2**(4), 492–516 (2011).
11. A. Wunder, K. Schoknecht, D. B. Stanimirovic, O. Prager, and Y. Chassidim, "Imaging blood-brain barrier dysfunction in animal disease models," *Epilepsia* **53**(6), 14–21 (2012).
12. J. Marcon, B. Gagliardi, S. Balosso, M. Maroso, F. Noe, M. Morin, M. Lerner-Natoli, A. Vezzani, and T. Ravizza, "Age-dependent vascular changes induced by status epilepticus in rat forebrain: implications for epileptogenesis," *Neurobiol. Dis.* **34**(1), 121–132 (2009).
13. S.M. Avtan, M. Kaya, N. Orhan, A. Arslan, N. Arican, A.S. Toklu, C. Gurses, I. Elmas, M. Kucuk, and B. Ahishali, "The effects of hyperbaric oxygen therapy on blood-brain barrier permeability in septic rats," *Brain Res.* **1412**, 63–72 (2011).
14. K. Schoknecht and H. Shalev, "Blood-brain barrier dysfunction in brain diseases: clinical experience," *Epilepsia* **53**(6), 7–13 (2012).
15. S. Swastika, A. Chaturvedi, P.P. Kaul, P. Hazari, S. Jha, S. Pal, B. Lal, P. Singh, A.K. Barthelemy, and Mishra, "Evaluation of BBB permeable nucleolipid (NLDPU): A di-C15-ketalised palmitone appended uridine as neuro-tracer for SPECT," *Int. J. Pharm.* **565**, 269–282 (2019).
16. P. Mossel, L. Garcia Varela, W. M. Arif, C. W. J. van der Weijden, H. H. Boersma, A. T. M. Willemsen, R. Boellaard, P. H. Elsinga, R. J. H. Borra, N. A. Colabufo, J. Toyohara, P. P. de Deyn, R. Dierckx, A. A. Lammertsma, A. L. Bartels, and G. Luurtsema, "Evaluation of P-glycoprotein function at the blood-brain barrier using [(18)F]MC225-PET," *Eur. J. Nucl. Med. Mol. Imaging* **48**(12), 4105–4106 (2021).
17. B. Guo, Z. Feng, D. H. Hu, S. D. Xu, E. Middha, Y. T. Pan, C. B. Liu, H. R. Zheng, J. Qian, Z. H. Sheng, and B. Liu, "Precise deciphering of brain vasculatures and microscopic tumors with dual NIR-II fluorescence and photoacoustic imaging," *Adv. Mater.* **31**(30), 1902504 (2019).
18. S. Lee, B. M. Kang, J. H. Kim, J. Min, H. S. Kim, H. Ryu, H. Park, S. Bae, D. Oh, M. Choi, and M. Suh, "Real-time in vivo two-photon imaging study reveals decreased cerebro-vascular volume and increased blood-brain barrier permeability in chronically stressed mice," *Sci. Rep.* **8**(1), 13064 (2018).
19. D. Ringuelet, M. A. Jeffrey, S. Dufour, P. L. Carlen, and O. Levi, "Continuous multi-modality brain imaging reveals modified neurovascular seizure response after intervention," *Biomed. Opt. Express* **8**(2), 873–889 (2017).
20. W. Feng, C. Zhang, T. T. Yu, O. Semyachkina-Glushkovskaya, and D. Zhu, "In vivo monitoring blood-brain barrier permeability using spectral imaging through optical clearing skull window," *J. Biophotonics* **12**(4), e201800330 (2019).
21. A. Rakymzhan, Y. D. Li, P. J. Tang, and R. K. Wang, "Procedure and protocols for optical imaging of cerebral blood flow and hemodynamics in awake mice," *Biomed. Opt. Express* **11**(6), 3288–3300 (2020).
22. P. Beard, "Biomedical photoacoustic imaging," *Interface Focus* **1**(4), 602–631 (2011).
23. L. V. Wang and J. J. Yao, "A practical guide to photoacoustic tomography in the life sciences," *Nat. Methods* **13**(8), 627–638 (2016).
24. W. Z. Qi, T. Jin, J. Rong, H. B. Jiang, and L. Xi, "Inverted multiscale optical resolution photoacoustic microscopy," *J. Biophotonics* **10**(12), 1580–1585 (2017).
25. Q. Chen, H. Guo, T. Jin, W. Z. Qi, H. K. Xie, and L. Xi, "Ultracompact high-resolution photoacoustic microscopy," *Opt. Lett.* **43**(7), 1615–1618 (2018).
26. W. Qin, Q. Gan, L. Yang, Y. C. Wang, W. Z. Qi, B. W. Ke, and L. Xi, "High-resolution in vivo imaging of rhesus cerebral cortex with ultrafast portable photoacoustic microscopy," *NeuroImage* **238**, 118260 (2021).
27. Y. C. Wang, G. R. Liang, F. Liu, Q. Chen, and L. Xi, "A long-term cranial window for high-resolution photoacoustic imaging," *IEEE Trans. Biomed. Eng.* **68**(2), 706–711 (2021).
28. B. Guo, J. Q. Chen, N. B. Chen, E. Middha, S. D. Xu, Y. T. Pan, M. Wu, K. Li, C. B. Liu, and B. Liu, "High-resolution 3D NIR-II photoacoustic imaging of cerebral and tumor vasculatures using conjugated polymer nanoparticles as contrast agent" *Adv. Mater.* **31**, 1808355 (2019).
29. W. Z. Qi, T. T. Li, C. Zhang, F. Liu, J. Wang, D. D. Chen, X. F. Fang, C. F. Wu, K. Li, and L. Xi, "Light-controlled precise delivery of NIR-responsive semiconducting polymer nanoparticles with promoted vascular permeability," *Adv. Healthc. Mater.* **10**(19), 2100569 (2021).
30. J. Lv, S. Li, J. D. Zhang, F. Duan, Z. Y. Wu, R. H. Chen, M. M. Chen, S. S. Huang, H. S. Ma, and L. M. Nie, "In vivo photoacoustic imaging dynamically monitors the structural and functional changes of ischemic stroke at a very early stage," *Theranostics* **10**(2), 816–828 (2020).
31. L. M. Liu, Q. Chen, L. W. Wen, C. Li, H. Qin, and D. Xing, "Photoacoustic therapy for precise eradication of glioblastoma with a tumor site blood-brain barrier permeability upregulating nanoparticle," *Adv. Func. Mater.* **29**(11), 1808601 (2019).
32. W. T. Li, R. H. Chen, J. Lv, H. K. Wang, Y. Liu, Y. Peng, Z. Y. Qian, G. Fu, and L. M. Nie, "In Vivo photoacoustic imaging of brain injury and rehabilitation by high-efficient near-infrared dye labeled mesenchymal stem cells with enhanced brain barrier permeability," *Adv. Sci.* **5**(2), 1700277 (2018).
33. G.R. Ullal, P. Satishchandra, and S.K. Shankar, "Hyperthermic seizures: an animal model for hot-water epilepsy," *Seizure* **5**(3), 221–228 (1996).

34. G. Ilbay, D. Sahin, and N. Ates, "Changes in blood-brain barrier permeability during hot water-induced seizures in rats," *Neurol. Sci.* **24**(4), 232–235 (2003).
35. N. Marchi, Q. Teng, C. Ghosh, Q. Fan, M.T. Nguyen, N.K. Desai, H. Bawa, P. Rasmussen, T.K. Masaryk, and D. Janigro, "Blood-brain barrier damage, but not parenchymal white blood cells, is a hallmark of seizure activity," *Brain Res.* **1353**, 176–186 (2010).
36. N. Marchi, G. Betto, V. Fazio, Q. Y. Fan, C. Ghosh, A. Machado, and D. Janigro, "Blood-brain barrier damage and brain penetration of antiepileptic drugs: role of serum proteins and brain edema," *Epilepsia* **50**(4), 664–677 (2009).
37. E. J. Kang, S. Major, D. Jorks, C. Reiffurth, N. Offenhauser, A. Friedman, and J. P. Dreier, "Blood-brain barrier opening to large molecules does not imply blood-brain barrier opening to small ions," *Neurobiol. Dis.* **52**, 204–218 (2013).
38. C. Yin, G. H. Wen, C. Liu, B. G. Yang, S. E. Lin, J. W. Huang, P. C. Zhao, S. H. D. Wong, K. Y. Zhang, X. Y. Chen, G. Li, X. H. Jiang, J. P. Huang, K. Y. Pu, L. D. Wang, and L. M. Bian, "Organic semiconducting polymer nanoparticles for photoacoustic labeling and tracking of stem cells in the second near-infrared window," *ACS Nano* **12**(12), 12201–12211 (2018).
39. D. F. Chen, W. Yuan, H. C. Park, and X. D. Li, "In vivo assessment of vascular-targeted photodynamic therapy effects on tumor microvasculature using ultrahigh-resolution functional optical coherence tomography," *Biomed. Opt. Express* **11**(8), 4316–4325 (2020).
40. E. A. van Vliet, S. da Costa Araujo, S. Redeker, R. van Schaik, E. Aronica, and J. A. Gorter, "Blood-brain barrier leakage may lead to progression of temporal lobe epilepsy," *Brain* **130**(2), 521–534 (2007).
41. E. A. van Vliet, G. Zibell, A. Pekcec, J. Schlichtiger, P. M. Edelbroek, L. Holtman, E. Aronica, J. A. Gorter, and H. Potschka, "COX-2 inhibition controls P-glycoprotein expression and promotes brain delivery of phenytoin in chronic epileptic rats," *Neuropharmacology* **58**(2), 404–412 (2010).
42. P. J. Robinson and S. I. Rapoport, "Size selectivity of blood-brain barrier permeability at various times after osmotic opening," *Am. J. Physiol.* **66**(2), 459 (1987).
43. T. Inoue, M. Fukui, S. Nishio, S. Kitamura, and H. Nagara, "Hyperosmotic blood-brain barrier disruption in brains of rats with an intracerebrally transplanted RG-C6 tumor," *J. Neurosurg.* **66**(2), 256–263 (1987).
44. Y. V. Tiwari, J. Lu, Q. Shen, B. Cerqueira, and T. Q. Duong, "Magnetic resonance imaging of blood-brain barrier permeability in ischemic stroke using diffusion-weighted arterial spin labeling in rats," *J. Cereb. Blood Flow Metab.* **37**(8), 2706–2715 (2017).
45. O. Prager, Y. Chassidim, C. Klein, H. Levi, I. Shelef, and A. Friedman, "Dynamic in vivo imaging of cerebral blood flow and blood-brain barrier permeability," *NeuroImage* **49**(1), 337–344 (2010).
46. S. Dufour, Y. Atchia, R. Gad, D. Ringuette, I. Sigal, and O. Levi, "Evaluation of laser speckle contrast imaging as an intrinsic method to monitor blood brain barrier integrity," *Biomed. Opt. Express* **4**(10), 1856–1875 (2013).
47. K. Kingwell, "Drug delivery: New targets for drug delivery across the BBB," *Nat. Rev. Drug Discov.* **15**(2), 84–85 (2016).
48. J. Xie, Z. Shen, Y. Anraku, K. Kataoka, and X. Chen, "Nanomaterial-based blood-brain-barrier (BBB) crossing strategies," *Biomaterials* **224**, 119491 (2019).
49. Z. K. Englander, H. J. Wei, A. N. Pouliopoulos, E. Bendau, P. Upadhyayula, C. I. Jan, E. F. Spinazzi, N. Yoh, M. Tazhibi, N. M. McQuillan, T. J. C. Wang, J. N. Bruce, P. Canoll, N. A. Feldstein, S. Zacharoulis, E. E. Konofagou, and C. C. Wu, "Focused ultrasound mediated blood-brain barrier opening is safe and feasible in a murine pontine glioma model," *Sci. Rep.* **11**(1), 6521 (2021).
50. L. Sosic, P. K. Selbo, Z. K. Kotkowska, T. M. Kundig, A. Hogset, and P. Johansen, "Photochemical internalization: light paves way for new cancer chemotherapies and vaccines," *Cancers* **12**(1), 165 (2020).
51. S. J. Madsen and H. Hirschberg, "Site-specific opening of the blood-brain barrier," *J. Biophotonics* **3**(5-6), 356–367 (2010).
52. M. A. O'Reilly, O. Hough, and K. Hynynen, "Blood-brain barrier closure time after controlled ultrasound-induced opening is independent of opening volume," *J. Ultrasound Med.* **36**(3), 475–483 (2017).
53. G. Bar-Klein, L. P. Cacheaux, L. Kamintsky, O. Prager, I. Weissberg, K. Schoknecht, P. Cheng, S. Y. Kim, L. Wood, U. Heinemann, D. Kaufer, and A. Friedman, "Losartan prevents acquired epilepsy via TGF-beta signaling suppression," *Ann. Neurol.* **75**(6), 864–875 (2014).
54. A. K. Schmitz, A. Grote, A. Raabe, H. Urbach, A. Friedman, M. von Lehe, A. J. Becker, and P. Niehusmann, "Albumin storage in neoplastic astroglial elements of gangliogliomas," *Seizure* **22**(2), 144–150 (2013).
55. B. Ahishali, M. Kaya, N. Orhan, N. Arican, O. Ekizoglu, I. Elmas, M. Kucuk, G. Kemikler, R. Kalayci, and C. Gurses, "Effects of levetiracetam on blood-brain barrier disturbances following hyperthermia-induced seizures in rats with cortical dysplasia," *Life Sci.* **87**(19-22), 609–619 (2010).